Whispering-gallery-mode cavity for terahertz pulses

Jiangquan Zhang and D. Grischkowsky

School of Electrical and Computer Engineering and Center for Laser and Photonics Research, Oklahoma State University, Stillwater, Oklahoma 74078

Received January 6, 2003; revised manuscript received May 16, 2003

We report an experimental and theoretical study of whispering-gallery-mode propagation of subpicosecond terahertz pulses in a dielectric cylinder coupled by means of a dielectric slab waveguide. We observed repetitive cavity pulses from this structure for which the output pulse shapes were determined by the multi-whispering-gallery-mode coupling into the cylinder. A coupled-mode theory derived for this cylindrical system and coupling structure gives reasonably good agreement with the experiment in both the frequency and time domains. © 2003 Optical Society of America

OCIS codes: 230.0230, 250.5530, 260.2110, 320.5390, 320.7090.

1. INTRODUCTION

The term whispering-gallery mode (WGM) describes the electromagnetic wave that circulates around the inner surface of a dielectric sphere or cylinder as the result of total internal reflection.[1] With size flexibility, mechanical stability, adaptability to integrated circuits, and very high Q value, WGM resonators are widely used for basic research and for applications.[2–12] At millimeter wavelengths, conventional cylindrical dielectric resonators that operate in their TE or TM modes have quite small dimensions, and therefore are difficult to machine. Also, their Q factors are strongly reduced.[13] WGM resonators, however, can overcome this serious defect, and are hence very suitable for millimeter-wavelength integrated circuits. Consequently, WGM resonators have been used for frequency filters[2] and power combiners[3] in millimeter-wavelength integrated circuits. In the optical range, the WGM resonator is usually a dielectric sphere.[4–10] The high Q value guarantees the building up of the electromagnetic field of a certain frequency, which is very important in the applications of frequency selection,[4] spectroscopy,[5] nonlinear optics,[6] the microlaser cavity,[7] and parameter detection.[8] At telecommunication wavelengths, similar microring resonators have been reported for frequency filtering and modulation.[9]

A WGM resonator is usually excited by the external evanescent fields of a coupler, which can be a dielectric prism,[4,5] an optical fiber,[7,10] microstrip transmission lines,[11] or a dielectric waveguide.[12] When the electromagnetic wave of the coupler passes through the coupler–resonator contact region, part of the field is coupled into the resonator and propagates around its inner surface. In the case of a cw coupling source, the coherence condition must be met for constructive interference, and only a set of discrete frequencies can satisfy this condition. These resonant frequencies are determined by the dimensions and coupling condition of the dielectric resonator and the polarization of the coupling source.

In recent years, terahertz (THz) technology has attracted considerable research effort, and has become a bridge connecting microwave technology at the low-frequency end with optical technology at the high-frequency end. Many research topics in these two frequency regions have been expanded to THz range, one of which is guided-wave propagation. Recent progress in THz waveguide studies[14–17] has paved the way for guided-wave propagation and circuit interconnection of THz radiation. The advancing technology and expanding applications of THz radiation will soon require the use of the THz-WGM resonator.

Unlike a cw laser source, a beam of subpicosecond THz pulses consists of a continuous range of frequency components. The standard THz-time-domain spectroscopy system[18] is able to record both the amplitude and phase information of such pulses. Although most of the related optical WGM studies use a cw laser, a time-resolved measurement of WGM pulse propagation in spheres has been demonstrated by use of a pulsed optical laser as the coupling source.[19] On the basis of techniques developed in THz waveguide studies,[14–17] we have reported the first observation of WGM propagation of THz pulses.[20] Here we give a detailed explanation of our experiment and the theoretical analysis of the dielectric-slab–cylinder coupling structure reported in Ref. 20. The experiment shows strong coupling between the dielectric-slab waveguide and the cylinder and demonstrates the propagation properties of the THz-WGM pulse. We give the mode solutions for this system and derive the coupled-mode equations (CMEs) to analyze our slab–cylinder coupling structure. The theory explains the experiment well and can be used for related future studies.

2. EXPERIMENT

The optoelectronic THz system used for our experiment is shown in Fig. 1. The THz pulse is generated by a coplanar stripline biased under high voltage and excited by laser pulses from a Ti:sapphire mode-locked laser. Two paraboloidal mirrors are used for steering and collimating

the THz beam. For a typical THz-time-domain spectroscopy measurement, the sample under investigation is placed between the two paraboloidal mirrors. In our case, the sample is a slab–cylinder coupling structure along with the focusing lenses and sandwiching metal plates for the slab, which is shown enlarged in Fig. 2. The slab waveguide and the cylinder are both made of high-resistivity silicon with a refractive index $n_{Si} = 3.417$[18] and dimensions of 17.5 mm (length, z) by 100 μm (thickness, y) by 12.5 mm (height, x) and 5 mm (diameter) by 10 mm (height, x), respectively. The two aluminum sandwiching plates are both 18 mm (length, z) by 25 mm (height, x), each having a window of 3.2 mm (length, z) by 17 mm (height, x) in the middle. To place the cylinder in contact with the slab waveguide, the window of the coupling plate is carefully milled out using a 6.2-mm ball-end bit. A 5-mm-diameter aperture is placed before the left-hand lens to confine the incoming beam. To eliminate the effects of water vapor, the whole system is enclosed in an airtight box that is purged and kept at a positive pressure by dry air during data collection.

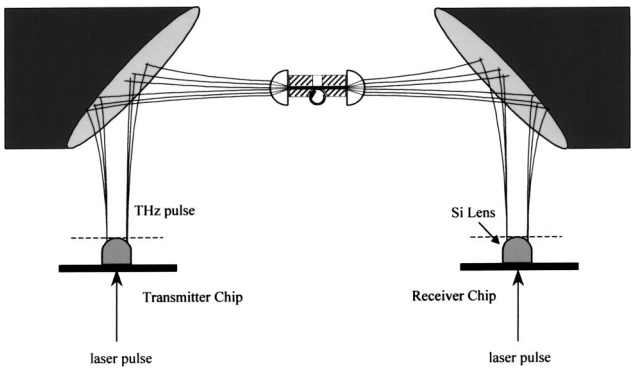

Fig. 1. Experimental setup.

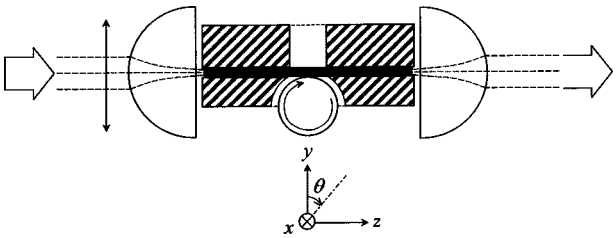

Fig. 2. Cross section of the slab–cylinder coupling structure.

The incoming y-polarized THz pulse is coupled in and out of the coupling structure by the two cylindrical lenses. In the window area, the THz pulse propagates in the dispersive TM_0 mode of the dielectric-slab waveguide.[15] On the left and right sides of the coupling structure, the two aluminum plates and the sandwiched silicon slab form the parallel-metal-plate waveguide. If there is no residual air between the slab and the metal plates, the THz pulse will propagate in the TEM mode with no frequency chirp and no group-velocity dispersion.[16] In the experiment it is difficult to obtain intimate contact between the silicon slab and the metal plates, so that an air gap of a few micrometers may exist between the silicon slab and the metal plates. In this case a pure TEM mode does not exist in the metal guide. However, since the coupling to the cylinder occurs only in the window area (the slab-waveguide region), in the theoretical section we need focus only on the modes of the slab waveguide.

When the cylinder is brought into contact with the slab, part of the THz pulse is coupled into the cylinder as a superposition of WGM modes and propagates around the cylinder. A cavity pulse train is obtained as the coupling occurs each time the circulating THz-WGM pulse reaches the contact region and part of it is coupled back to the slab waveguide and detected as a cavity pulse.

3. EXPERIMENTAL RESULTS

The time-domain output pulse of the above system is shown in Figs. 3(a) and 3(b) for the reference scan (without cylinder) and the sample scan (with cylinder in contact with silicon slab), respectively. As described in Ref. 20, pulses 1a and 1b are the main transmitted pulses, while 2a, 2b, 3a, and 3b are the reflection pulses from the cylindrical lenses. The first two cavity pulses are de-

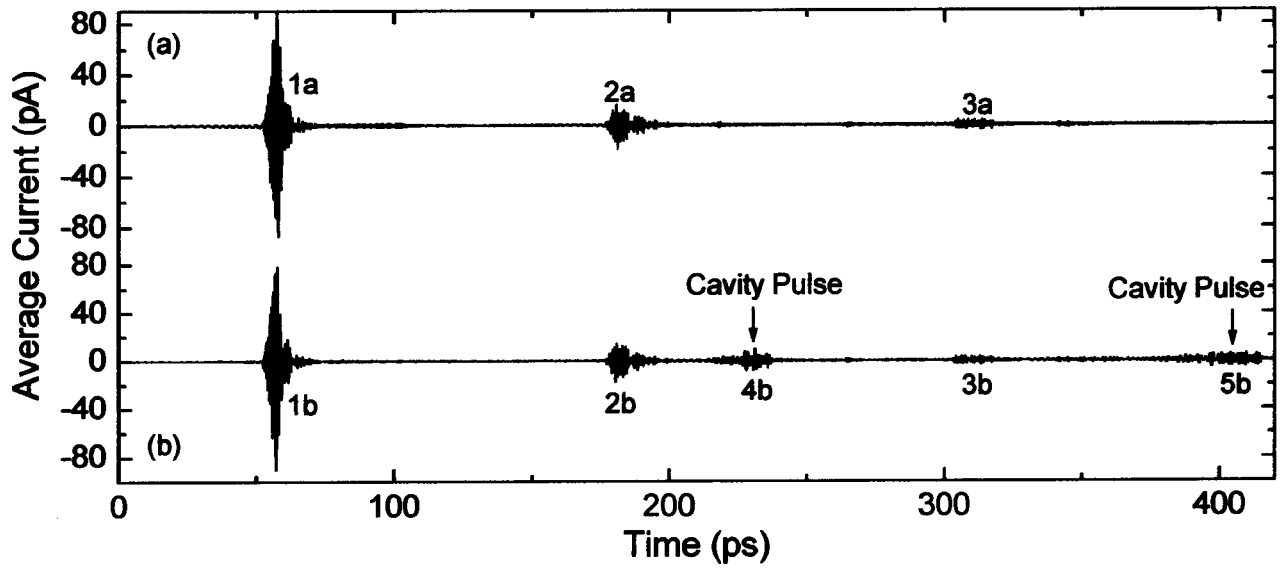

Fig. 3. Measured time domain pulses: (a) reference scan without cylinder, (b) sample scan with the cylinder in contact with the slab waveguide.

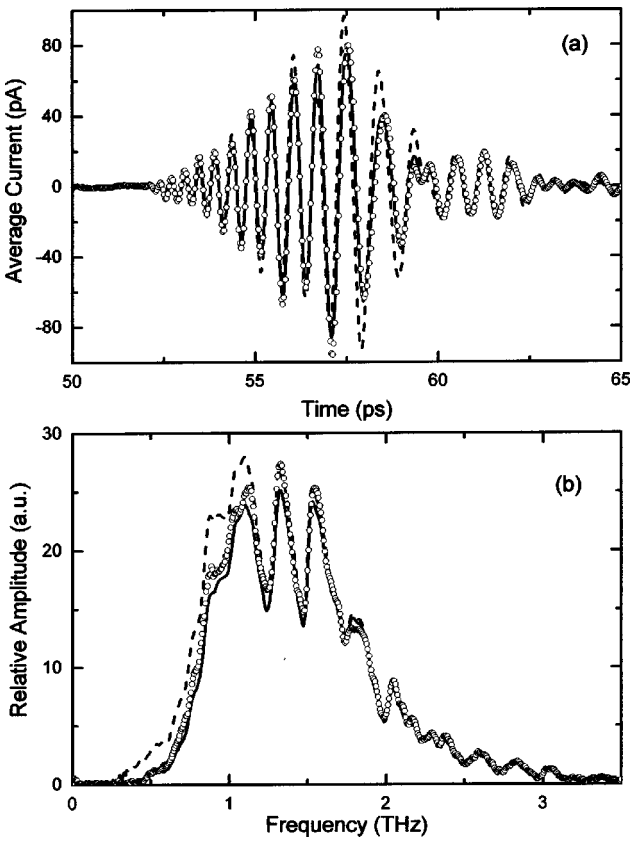

Fig. 4. (a) Main transmitted pulses of Fig. 3 and, (b) their corresponding spectra. The dashed curves represent the reference scan, the open circles represent the sample scan, and the solid curves are the calculation results for the sample scan.

noted 4b and 5b, which are identified by their corresponding time delays relative to pulse 1b.[20]

Figure 4(a) shows magnifications of Figs. 3(a) and 3(b) for the main transmitted pulses 1a and 1b. Figure 4(b) shows their corresponding spectra. The oscillations in their spectra are a result of the reflection between the planar surfaces of the cylindrical lenses and the entrance and exit surfaces of the silicon slab, which are separated by approximately 0.7 mm; the spectra show the single-mode propagation of pulses 1a and 1b. The main transmitted pulse retains most of its amplitude and oscillation features when the cylinder is brought into contact with the slab waveguide. However, with the cylinder in contact, the pulse loses part of its energy at lower frequencies, indicating strong coupling between the slab and the cylinder. This can also be seen in the time domain shown in Fig. 3. The small oscillations in the leading part of pulse 1a correspond to the lower-frequency components having the fastest group velocities of the slab TM_0 mode.[15] These oscillations almost disappear when the cylinder is brought into contact, as most of these frequency components are then coupled into the cylinder.

Figures 5(a) and 5(b) are magnifications of Fig. 3 for the first and the second cavity pulses, respectively. Their respective spectra are shown in Figs. 6(a) and 6(b). Although the incoming THz pulse propagates in the single TM_0 mode in the slab waveguide, the spectra of the cavity pulses show oscillations which indicate the multimode feature of the THz-WGM pulse.[14,20] This is due to the situation that the single slab TM_0 mode is coupled into several WGMs of the cylinder.

4. COUPLED-MODE EQUATIONS (CMEs)

We now derive the CMEs for the slab–cylinder coupling system shown in Fig. 7. We assume that the system is uniform in the x direction so that the problem simplifies to two dimensions. Consider two sets of frequency-domain field solutions ($\mathbf{E}_1$, $\mathbf{H}_1$) and ($\mathbf{E}_2$, $\mathbf{H}_2$) in two different dielectric media $\varepsilon_1(r, \theta)$ and $\varepsilon_2(r, \theta)$ that satisfy Maxwell's equations and the boundary conditions, and are located in the same physical space as Fig. 7. Here, the field quantities contain the implicit time dependence $\exp(-i\omega t)$ and $\varepsilon_1(r, \theta)$ and $\varepsilon_2(r, \theta)$ represent the spatial distribution of relative permittivities for the two media. From the vector identities and Maxwell's equations, it is easy to obtain the following relation[21–23]:

$$\nabla \cdot (\mathbf{E}_1 \times \mathbf{H}_2 - \mathbf{E}_2 \times \mathbf{H}_1) = ik\sqrt{\frac{\epsilon_0}{\mu_0}}(\varepsilon_2 - \varepsilon_1)\mathbf{E}_1 \cdot \mathbf{E}_2, \quad (1)$$

where k is the free-space wave number and ϵ_0 and μ_0 are the permittivity and permeability of free space, respectively. The above relation is derived directly from Maxwell's equations and is accurate for any two sets of field solutions. If we multiply both sides of Eq. (1) by r and

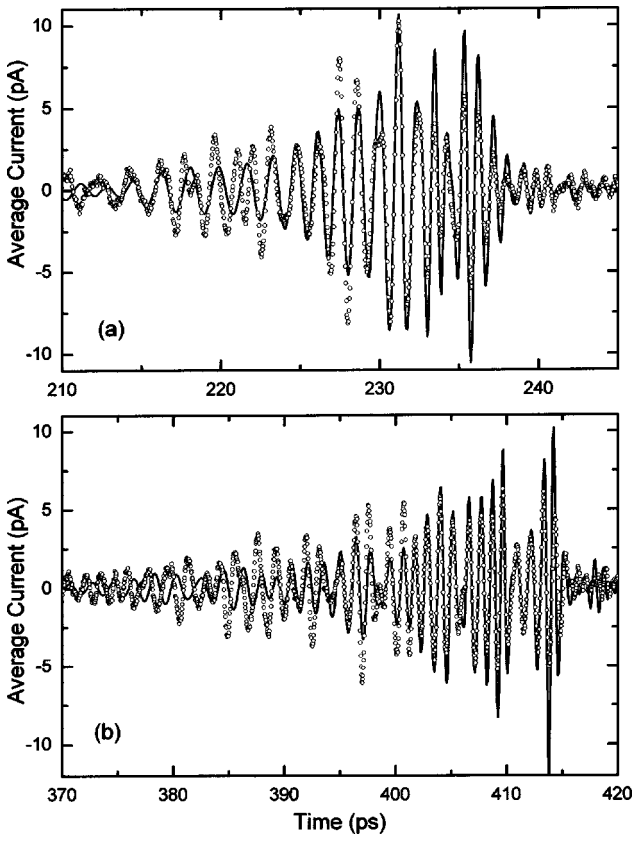

Fig. 5. Output pulses for (a) the first and, (b) the second cavity pulses (4b and 5b, respectively). The solid curves are calculation results and the open circles represent the experiment.

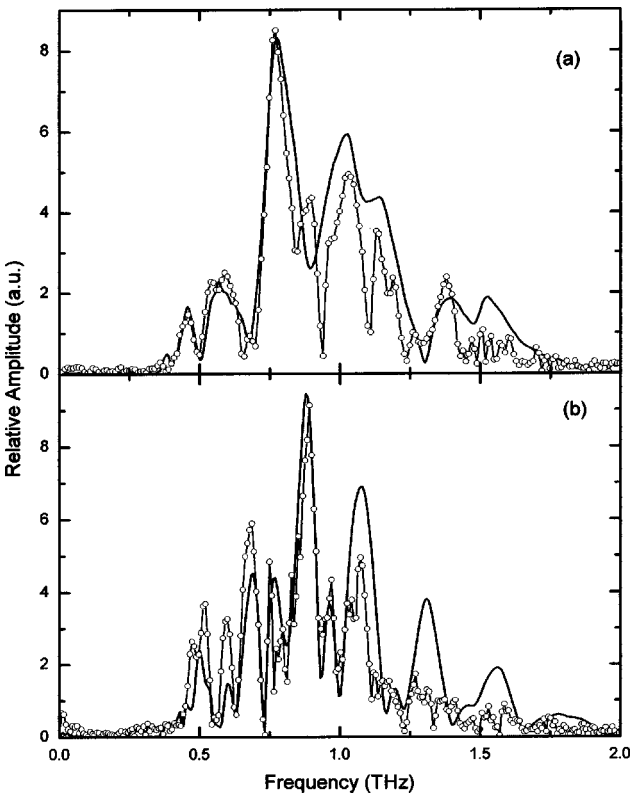

Fig. 6. Spectra of (a) the first and (b) the second cavity pulses (4b and 5b, respectively). The heavy curves are calculation results and the light curves with open circles represent the experiment.

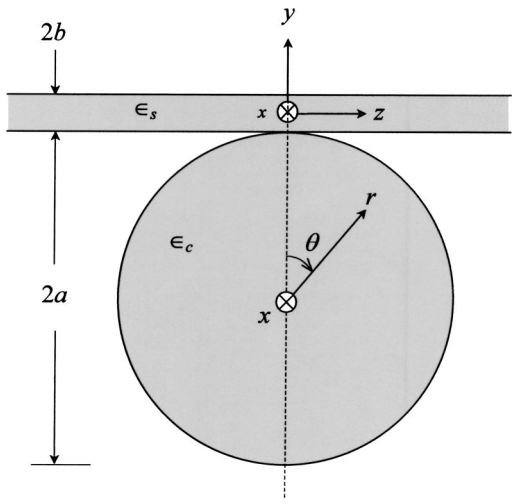

Fig. 7. Coordinate system of the slab–cylinder coupling structure.

integrate along the r direction, in cylindrical coordinates we obtain the so-called reciprocity theorem[24,25]:

$$\frac{\mathrm{d}}{\mathrm{d}\theta}\int_0^\infty (\mathbf{E}_1 \times \mathbf{H}_2 - \mathbf{E}_2 \times \mathbf{H}_1)\cdot\hat{\theta}\,\mathrm{d}r = ik\sqrt{\frac{\epsilon_0}{\mu_0}}\int_0^\infty (\varepsilon_2 - \varepsilon_1)\mathbf{E}_1 \cdot \mathbf{E}_2 r\,\mathrm{d}r, \quad (2)$$

where the caret $\hat{}$ over θ indicates a unit vector. Note that this exact relationship differs slightly from the previous approximate form.[24,25]

We now apply this relation to our slab–cylinder system to derive the CMEs. It should be understood that Eq. (2) is valid for any solution of the slab and cylinder and for a linear superposition of such solutions. We use the subscripts s and c to indicate the isolated slab and cylinder systems, respectively, and capital T to indicate the coupled slab–cylinder system as a whole. As shown in Fig. 7, for the isolated cylinder system, the spatial relative permittivity is

$$\varepsilon_c(r,\theta) = \begin{cases} \epsilon_c & \text{inside cylinder,} \\ 1 & \text{outside cylinder.} \end{cases} \quad (3)$$

For the isolated slab system, this function is

$$\varepsilon_s(r,\theta) = \begin{cases} \epsilon_s & \text{inside slab,} \\ 1 & \text{outside slab.} \end{cases} \quad (4)$$

In Eqs. (3) and (4), ε_c and ε_s are constants and represent the relative permittivities of the dielectric cylinder and slab, respectively. For the coupled slab–cylinder system, the spatial relative permittivity is

$$\varepsilon_T(r,\theta) = \begin{cases} \epsilon_c & \text{inside cylinder,} \\ \epsilon_s & \text{inside slab,} \\ 1 & \text{in air.} \end{cases} \quad (5)$$

Corresponding to the spatial relative permittivities shown in Eqs. (3)–(5), the field solutions are ($\mathbf{E}_c$, $\mathbf{H}_c$), ($\mathbf{E}_s$, $\mathbf{H}_s$), and ($\mathbf{E}_T$, $\mathbf{H}_T$), respectively. Note that the first two solutions are known (see Appendix A). The purpose of this section is to give a modal solution for the third one. We first consider the coupling between a single slab mode and a single cylinder mode. In cylindrical coordinates, we form the total field for the coupled system by the modal expansion of the two isolated systems as[23,24]

$$\mathbf{E}_T(r,\theta) = a_s(\theta)\left[\mathbf{E}_s^t(r,\theta) + \frac{\varepsilon_s}{\varepsilon_T}\hat{\theta}E_s^\theta(r,\theta)\right] + a_c(\theta)\left[\mathbf{E}_c^t(r,\theta) + \frac{\varepsilon_c}{\varepsilon_T}\hat{\theta}E_c^\theta(r,\theta)\right], \quad (6a)$$

$$\mathbf{H}_T(r,\theta) = a_s(\theta)[\mathbf{H}_s^t(r,\theta) + \hat{\theta}H_s^\theta(r,\theta)] + a_c(\theta)[\mathbf{H}_c^t(r,\theta) + \hat{\theta}H_c^\theta(r,\theta)], \quad (6b)$$

where the superscripts t and θ indicate the transverse and θ components, respectively, and $a_s(\theta)$ and $a_c(\theta)$ are the modal amplitudes for the slab and cylinder modes, respectively. Here the Cartesian coordinates of the slab have been transformed to the cylindrical coordinates of the cylinder. The goal of this analysis is to solve for $a_s(\theta)$ and $a_c(\theta)$ using the reciprocity relation [Eq. (2)]. For the two sets of field solutions and relative permittivities required in this relation, we choose the coupled slab–cylinder system as one set; for the other set, we choose the individual isolated system with the fields propagating in the $-\theta$ direction (these are also the field solutions of the individual systems; see Appendix B). We obtain from Eq. (2)

$$\frac{\mathrm{d}}{\mathrm{d}\theta}\int_0^\infty (\mathbf{E}_T \times \mathbf{H}_s^- - \mathbf{E}_s^- \times \mathbf{H}_T)\cdot\hat{\theta}\mathrm{d}r = ik\sqrt{\frac{\epsilon_0}{\mu_0}}\int_0^\infty (\varepsilon_s - \varepsilon_T)\mathbf{E}_T \cdot \mathbf{E}_s^- r\mathrm{d}r, \quad (7a)$$

$$\frac{\mathrm{d}}{\mathrm{d}\theta}\int_0^\infty (\mathbf{E}_T \times \mathbf{H}_c^- - \mathbf{E}_c^- \times \mathbf{H}_T)\cdot\hat{\theta}\mathrm{d}r = ik\sqrt{\frac{\epsilon_0}{\mu_0}}\int_0^\infty (\varepsilon_c - \varepsilon_T)\mathbf{E}_T \cdot \mathbf{E}_c^- r\mathrm{d}r, \quad (7b)$$

where the superscript $-$ indicates the $-\theta$ direction. Substituting the corresponding field expressions from Appendix B, we get the following CMEs:

$$\frac{\mathrm{d}}{\mathrm{d}\theta}[P_{ss}(\theta)a_s(\theta) + P_{sc}(\theta)a_c(\theta)] = iC_{ss}a_s(\theta) + iC_{sc}a_c(\theta), \quad (8a)$$

$$\frac{\mathrm{d}}{\mathrm{d}\theta}[P_{cs}(\theta)a_s(\theta) + P_{cc}(\theta)a_c(\theta)] = iC_{cs}a_s(\theta) + iC_{cc}a_c(\theta), \quad (8b)$$

where the coupling coefficients are defined as

$$P_{pq}(\theta) = \frac{1}{4}\int_0^\infty \exp(i\Delta\Phi_{pq})(\mathbf{e}_p^t \times \mathbf{h}_q^t + \mathbf{e}_q^t \times \mathbf{h}_p^t)\cdot\hat{\theta}\mathrm{d}r, \quad (9a)$$

$$C_{pq}(\theta) = \frac{k}{4}\sqrt{\frac{\epsilon_0}{\mu_0}}\int_0^\infty \Delta\varepsilon_p \exp(i\Delta\Phi_{pq}) \times \left(\mathbf{e}_p^t \cdot \mathbf{e}_q^t - \frac{\varepsilon_q}{\varepsilon_T}e_p^\theta e_q^\theta\right) r\mathrm{d}r, \quad (9b)$$

with the subscripts $p,q = s,c$; $\Delta\varepsilon_p(r,\theta) = \varepsilon_T(r,\theta) - \varepsilon_p(r,\theta)$; and the phase difference $\Delta\Phi_{pq}(r,\theta) = \Phi_q(r,\theta) - \Phi_p(r,\theta)$ (where $\Phi_s(r,\theta) = \beta z(r,\theta)$ and $\Phi_c(r,\theta) = l\theta$, with β the propagation constant of the slab mode and l the angular propagation constant of the WGM). The lower case $\mathbf{e}(e)$ and $\mathbf{h}(h)$ represent the normalized field solutions as shown in Appendix B. Note that by definition of the normalization factors of relations (A4) and (A9),

$$P_{ss} \approx P_{cc} = 1. \quad (10)$$

It is worthwhile to point out that for the slab modes, as long as the origin of the cylindrical coordinates is away from the slab, which is true in our case, this is a very good approximation. In the above, we used specific combinations of the field solutions to derive the CMEs. Although other combinations could be put into the reciprocity relation of Eq. (2), the total field has to be used in order to get the CMEs, and the use of the individual field solutions in the $-\theta$ direction assures that the coupling coefficients have the simplest forms. In fact, the terms in the bracket of the left-hand side of Eq. (8a) represent the total modal amplitude of the slab mode, which is given as the projection of the total field into the slab mode, while the right-hand side is the excitation by an equivalent current induced by the cylinder and the total field. (A detailed explanation of the induced current can be found in Chapter 22 of Ref. 22.) Eq. (8b) can be explained similarly.

Equations (8a) and (8b) are the CMEs for the coupling between a single slab mode and a single cylindrical WGM. For our slab–cylinder system, the modes involved in the coupling are the single slab TM_0 mode and several cylindrical WGMs. Following similar procedure, the multimode CMEs can be derived quite generally for the coupling between a single slab TM_0 mode and multiple WGMs as

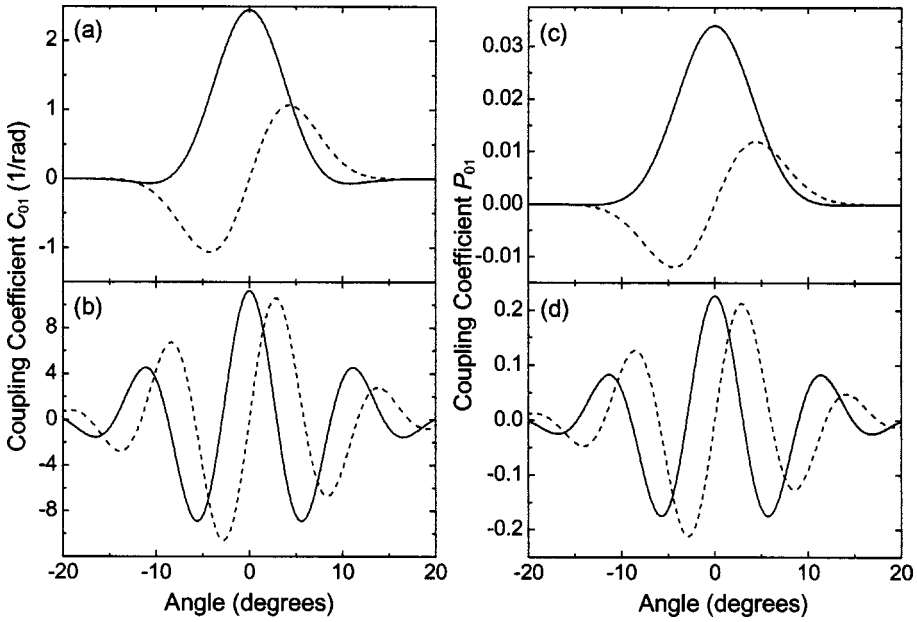

Fig. 8. Coupling coefficients for the slab TM_0 mode and WG_1 mode at 1.0 and 0.5 THz. The solid curves are real parts and the dashed curves represent imaginary parts. (a) C_{01} at 1 THz. (b) C_{01} at 0.5 THz. (c) P_{01} at 1 THz. (d) P_{01} at 0.5 THz.

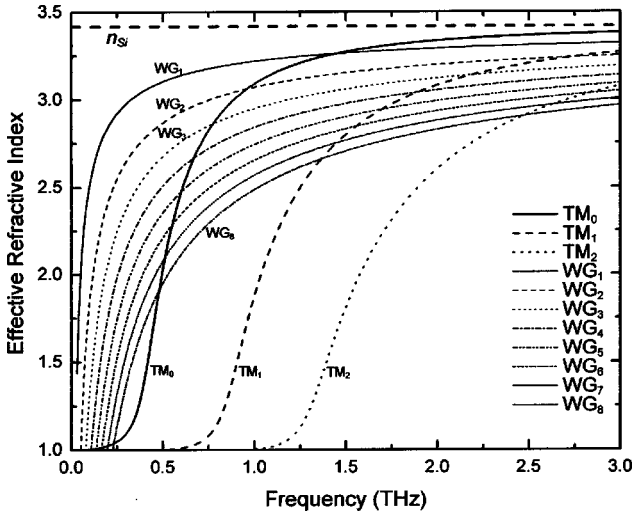

Fig. 9. Effective refractive indices of the slab TM modes and the cylindrical WGMs. The straight dashed line indicates the essentially constant refractive index of silicon $n_{Si} = 3.417$.

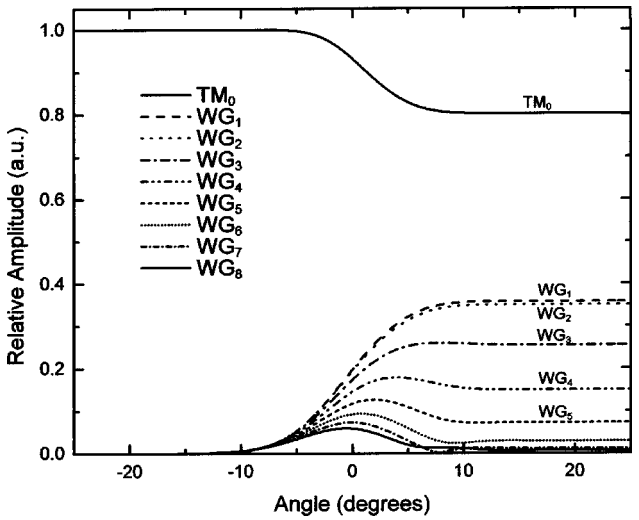

Fig. 10. Amplitude evolution during the coupling process at 1.0 THz when the slab TM_0 mode is initially excited.

$$\frac{d}{d\theta}\sum_{n=0}^{N} P_{mn}(\theta)a_n(\theta) = i\sum_{n=0}^{N} C_{mn}(\theta)a_n(\theta), \qquad (11)$$

where N is the total number of WGMs; $m, n = 0, 1,..., N$ are mode numbers; a_n is the modal amplitude of the nth mode; and P_{mn} and C_{mn} are coupling coefficients defined in Eqs. (9a) and (9b). For simplicity, we use subscript 0 to indicate the slab TM_0 mode and $n = 1, 2,...$ to indicate the nth WGM (denoted as WG_n). Eq. (11) for the CMEs can be written in the matrix form

$$\frac{d}{d\theta}[P(\theta)A(\theta)] = iC(\theta)A(\theta), \qquad (12)$$

where $A(\theta)$ is a single-column matrix with the elements $a_0(\theta)$, $a_1(\theta),...a_N(\theta)$. Note that the orthogonality of WGMs is determined by the overlap integral of the transverse fields, so, in our case, the modes with different radial number m are orthogonal, thus the coefficients $P_{mn} \approx 0$ and $C_{mn} \approx 0$ if m and n refer to different WGMs. This allows us to reduce the matrices as follows:

$$P(\theta) = \begin{bmatrix} 1 & P_{01} & P_{02} & \cdots & P_{0N} \\ P_{10} & 1 & 0 & \cdots & 0 \\ P_{20} & 0 & 1 & \cdots & 0 \\ \vdots & \vdots & \vdots & \ddots & \vdots \\ P_{N0} & 0 & 0 & \cdots & 1 \end{bmatrix},$$

$$C(\theta) = \begin{bmatrix} C_{00} & C_{01} & C_{02} & \cdots & C_{0N} \\ C_{10} & C_{11} & 0 & \cdots & 0 \\ C_{20} & 0 & C_{22} & \cdots & 0 \\ \vdots & \vdots & \vdots & \ddots & \vdots \\ C_{N0} & 0 & 0 & \cdots & C_{NN} \end{bmatrix}. \qquad (13)$$

5. NUMERICAL CALCULATION

A. Coupling Coefficients

Putting the integrals in Eqs. (9a) and (9b) into practice, we show in Fig. 8 the coupling coefficients for slab TM_0 and cylindrical WG_1 mode (C_{01} and P_{01}) at 0.5 and 1.0 THz for our coupling system. Note that by definition, C_{mn} has the dimension of 1/angle. It is seen that at 0.5 THz, the coupling coefficients show an oscillation feature that results from the two modes' having a very large phase mismatch. As shown in Fig. 9, the difference between the effective refractive indices (see Appendix A) of TM_0 and WG_1 modes at 0.5 THz is much larger than that at 1 THz. This difference is reflected in Eqs. (9a) and (9b) and causes the oscillations in the coupling coefficients. These oscillations will affect the final coupling results.

B. Frequency-Transfer Functions

The main transmitted pulse 1b of the sample scan and the cavity pulses 4b and 5b can be viewed in the frequency domain as linear transformations of the main transmitted pulse 1a of the reference scan,[20] i.e., $A_j(\omega) = H_j(\omega)A_r(\omega)$, where $A_j(\omega)$ stands for the complex spectrum of the main transmitted pulse 1b of the sample scan ($j = 0$) and that of the first two cavity pulses ($j = 1,2$), $H_j(\omega)(j = 0,1,2)$ are their corresponding complex frequency-transfer functions, and $A_r(\omega)$ is the complex spectrum of the main transmitted pulse 1a of the reference scan. The CMEs have to be solved to obtain the transfer functions. As described in Section 2 and Ref. 20, the coupling occurs in several steps. According to the nature of the coupling, different sets of CMEs are used for different steps.

For the first coupling step, the THz pulse is coupled from the single slab TM_0 mode into the cylinder as a composition of several WGMs. In this step, the power is simultaneously injected into all the WGMs and the single slab TM_0 is depleted, so we use Eq. (12) to calculate the multimode coupling, and we set the initial modal amplitudes $a_{0i} = 1$ for the slab TM_0 mode and $a_{mi} = 0$ ($m \geq 1$) for the WG_m modes. Here the subscript i indicates the initial value. The fourth order Runge–Kutta method is used to solve Eq. (12) numerically, and we obtain the frequency-dependent, final, coupled, modal amplitudes

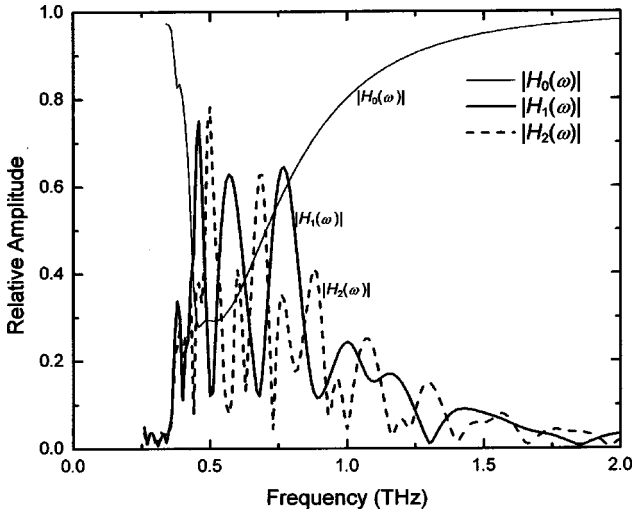

Fig. 11. Amplitude transfer functions of the main transmitted pulse $|H_0(\omega)|$ and the cavity pulses $|H_1(\omega)|$ and $|H_2(\omega)|$.

$a^s_{0f}(\omega)$ (for slab TM_0 mode) and $a^s_{mf}(\omega)$ (for WG_m mode), where the superscript s indicates that the coupling is from slab TM_0 to cylinder (slab excited), and the subscript f indicates the final coupled amplitude. Here $a^s_{0f}(\omega)$ is actually the frequency-transfer function for the main transmitted pulse 1b of the sample scan, i.e., $H_0(\omega) = a^s_{0f}(\omega)$. Figure 10 shows the modal amplitude evolution of the modes during the coupling process at 1.0 THz when only the first 8 cylindrical WGMs are taken into account in the coupling. It is clearly seen that most of the coupling occurs at the vicinity of the contact, where the two fields have the greatest overlap. For higher-order modes ($m \geqslant 4$), since the phase mismatch is larger (refer to Fig. 9), the modal amplitudes oscillate in the coupling region. For mode number $m \geqslant 7$, the overall coupling effect is very small, so in the numerical calculation we will not take into account modes with $m > 8$.

After this coupling, the main pulse passes and there remains no electromagnetic wave propagation along the slab waveguide, but the coupled THz-WGM pulse circulates continuously about the cylinder. The second coupling occurs when this pulse arrives at the slab–cylinder contact region, where the slab waveguide modes are excited by the cylindrical WGMs. From Fig. 9, because of the poor phase-match condition, the coupling from the WGMs into the TM_2 mode is considered forbidden in the frequency range 0.3–2.5 THz; below 1.3 THz, only the TM_0 mode is excited with proper phase match; in the frequency range 1.3–2.5 THz, it is possible that both TM_0 and TM_1 modes are excited. In the last case, even though the TM_1 mode is excited, because of its antisymmetric nature it cannot be detected by the receiver.[14] From Fig. 9, the coupling to TM_0 is mainly from the first two or three WGMs in this frequency range, while the coupling into the TM_1 mode is mainly from the rest of the WGMs. Therefore, we only consider the coupling into the single TM_0 mode in the calculation of this coupling, since the coupling into the TM_1 mode will not affect the overall coupling results into the TM_0 mode. To further simplify the calculation, we assume that there is no "cross coupling" between the WGMs, i.e., the WGMs couple individually into the TM_0 mode and the coupling from the TM_0 mode back to the WGMs is so weak that the WGMs do not "see" each other during the coupling process. This allows us to use the single-mode CMEs (8a) and (8b) to calculate the coupling from the individual WGM to the slab TM_0 mode, and then combine the results to get the overall coupling effect.

For this calculation, we set the initial modal amplitudes $a_{0i} = 0$ for the slab TM_0 mode and $a_{mi} = 1\,(m \geqslant 1)$ for the WG_m modes. We obtain the frequency-dependent, final, coupled modal amplitudes $a^{cm}_{0f}(\omega)$ (for slab TM_0 mode) and $a^{cm}_{mf}(\omega)$ (for WG_m mode), where the superscript cm indicates that the coupling is from the cylindrical WG_m mode to slab (cylinder excited). The complex frequency-transfer function for the first cavity pulse is therefore written as[20]

$$H_1(\omega) = \sum_{m=1}^{N} a^s_{mf}(\omega) a^{cm}_{0f}(\omega) \exp[i 2\pi l_m(\omega)]. \quad (14)$$

In a similar fashion the transfer function for the second cavity pulse can be written as

$$H_2(\omega) = \sum_{m} a^s_{mf}(\omega) a^{cm}_{mf}(\omega) a^{cm}_{0f}(\omega) \exp[i 4\pi l_m(\omega)]. \quad (15)$$

Thus, given the noncoupled THz pulse 1a through the slab waveguide, we can calculate the transmitted pulse of the sample scan and the cavity pulses in both the frequency and time domains.[15,20]

C. Calculation Results

Figure 11 presents the amplitude part of the transfer functions for the three pulses. The calculated results are shown in Fig. 4 for the main transmitted pulse 1b, and in Fig. 5 (time domain) and Fig. 6 (frequency domain) for the cavity pulses, together with their corresponding experimental results. Figure 4 shows that the calculation gives excellent agreement for the main transmitted pulse, especially in the time domain. For the cavity pulses, the calculation results also give reasonably good agreement with the experiment. In the frequency domain, despite the discrepancy between theory and experiment for the minima and some detailed structures, the overall spectral structures of the cavity pulses are well explained by theory. In the time domain, the oscillation structures of the cavity pulses are precisely predicted by the theory. The rapidly oscillating structures in both the time and frequency domains involve constructive and destructive interference among the WGMs of the cylinder. This interference is determined by the complex product of coupling results $a^s_{mf} a^{cm}_{0f}$ and the relative phase difference between the WGMs caused by propagation around the cylinder. Since the THz-WGM pulses propagate a very long distance (in terms of wavelengths) before being coupled back to the slab waveguide and detected as the cavity pulses, it is obvious that any small error in the total phase calculation could lead to a large discrepancy in the phase difference between theory and experiment. In our opinion, the assumptions we used in the calculation, such as an infinite x dimension of the system and an infinite incoming beam height, all contribute to the discrep-

ancies. But in general, the theory gives a very good explanation of the propagation properties of the THz-WGM pulses and the coupling between the slab and the cylinder.

6. FURTHER DISCUSSION AND CONCLUSION

In the case of a cw coupling source, the optimal coupling efficiency usually requires destructive interference of the input field and re-emission from the resonator, which normally results in a gap between the coupler and the resonator.[26] In our case since the input pulse and the cavity pulse are separated in the time domain, it is evident that to obtain the maximum coupling, the cylindrical cavity should be placed in contact with the slab waveguide as the overlap of the cylinder and slab fields is maximum. When the air gap between the two is increased, the coupling will drop exponentially, as predicted by the theory.

In our experiment the cylindrical cavity has optically smooth surfaces and is made of high-resistivity silicon with very low absorption in the THz range. This ensures negligible absorption and scattering loss during the propagation of the WGM pulses. However, since the input beam and the cylinder have limited longitudinal dimensions, the THz-WGM pulses will spread out in the longitudinal direction during the propagation. In our opinion, this is the dominant loss of the isolated cavity. From the experimental results the ratio of the energies contained in the first two cavity pulses is 10:9.5, giving a rough estimate of the overall power decay of the WGM pulses in the cavity. Given the round-trip transit time of 180 ps, the exponential lifetime of energy in the cavity is 3.6 ns. However, this decay is due mainly to the coupling loss, and the estimate does not apply to individual frequency points because of the multimode interference nature of the coupling.

In conclusion, we have successfully coupled the THz pulse into a cylindrical cavity as a composition of the cylindrical WGMs. The strong coupling makes this structure a promising cavity coupling scheme in future THz circuits. The cavity pulses cover a continuous frequency range from 0.4 to 1.8 THz, compared with the discrete resonant frequencies for the cw case. This study also demonstrates the propagation properties of the THz-WGM pulse. Since the different WGMs travel with different group and phase velocities, the WGM pulse is broadened as it propagates; the first two cavity pulses have widths of 27 ps and 45 ps, respectively. However, the two pulses are well separated in the time domain since the round-trip delay of 180 ps is much longer than the pulse width. Also, different cavity pulses carry different spectral profiles as a result of interference between the modes upon detection.

The coupled-mode theory for multimode coupling developed for the slab–cylinder coupling structure gives a good explanation of the coupling between the slab and the cylinder and of the propagation properties of the THz-WGM pulses. The overall spectrum structure and the oscillation structure of the cavity pulses are well predicted by the theory.

In general, we have demonstrated the coupling and propagation properties of a WGM cavity for THz pulses. With the continuous effort and advances in the study of THz technology and its applications, this newly developed structure may find application in future THz technology.

APPENDIX A: MODE SOLUTIONS AND DISPERSION RELATIONS

1. Even-Numbered TM Modes of Dielectric Slab Waveguide

Figure 7 shows the dielectric slab waveguide of thickness $2b$ and refractive index $n_s(n_s^2 = \epsilon_s)$ in air. Since the input THz beam is y polarized and symmetric, only even-numbered TM modes are excited in the slab waveguide. The nonvanishing field components of the normalized, even TM modes can be written inside the waveguide $(|y| < b)$ as[22]

$$h_{sm}^{x}(y) = -\frac{1}{\sqrt{N_{sm}}}\frac{k{n_s}^2}{\beta_m}\sqrt{\frac{\epsilon_0}{\mu_0}}\frac{\cos U_m Y}{\cos U_m},$$

$$e_{sm}^{y}(y) = \frac{1}{\sqrt{N_{sm}}}\frac{\cos U_m Y}{\cos U_m},$$

$$e_{sm}^{z}(y) = -\frac{1}{\sqrt{N_{sm}}}\frac{i{n_s}^2}{b}\frac{W_m}{\beta_m}\frac{\sin U_m Y}{\sin U_m}; \tag{A1}$$

and outside the waveguide $(|y| > b)$ as

$$h_{sm}^{x}(y) = -\frac{1}{\sqrt{N_{sm}}}\frac{k{n_s}^2}{\beta_m}\sqrt{\frac{\epsilon_0}{\mu_0}}\frac{\exp(-W_m|Y|)}{\exp(-W_m)},$$

$$e_{sm}^{y}(y) = \frac{{n_s}^2}{\sqrt{N_{sm}}}\frac{\exp(-W_m|Y|)}{\exp(-W_m)},$$

$$e_{sm}^{z}(y) = -\frac{1}{\sqrt{N_{sm}}}\frac{i{n_s}^2}{b}\frac{W_m}{\beta_m}\frac{Y}{|Y|}\frac{\exp(-W_m|Y|)}{\exp(-W_m)}; \tag{A2}$$

where the subscript m indicates a specific mode, the superscripts x, y, and z indicate the corresponding components, k is the wave vector in free space, and β_m is the propagation constant. For simplicity, the phase factor $\exp(i\beta_m z - i\omega t)$ has been omitted. Other parameters in the above equations are defined as:

$$U_m = b\sqrt{k^2{n_s}^2 - {\beta_m}^2}, \quad W_m = b\sqrt{{\beta_m}^2 - k^2},$$
$$Y = y/b. \tag{A3}$$

The normalization factor N_{sm} is determined by[22]

$$\tfrac{1}{2}\int_{-\infty}^{\infty}\mathbf{e}_{sm} \times \mathbf{h}_{sm} \cdot \hat{z}\,dx = 1. \tag{A4}$$

Applying the boundary conditions, we get the following eigenvalue equation:

$$ {n_s}^2 W_m = U_m \tan U_m . \tag{A5}$$

Solving (A5) for β_m, we obtain a set of solutions (modes). The modes are numbered by the number of zeros of the

magnetic field inside the slab waveguide in the y direction. The normalized field patterns of the slab TM modes can be found in Ref. 25.

For the purpose of deriving the propagation constant, the eigenvalue equation for the odd TM modes is also given here as[22]

$$n_s{}^2 W_m = -U_m \cot U_m . \tag{A6}$$

2. Cylindrical Whispering-Gallery Modes

Inside the cylindrical cavity, only the modes with $E^x = 0$ and $H^\theta = 0$ are excited during the coupling process. Figure 7 shows the cross section of the cylinder with radius a and refractive index $n_c (n_c^2 = \epsilon_c)$ surrounded by air. The field solution for the WGMs can be written inside the cylinder $(r < a)$ as[27]

$$h_{cm}^x(r) = \frac{1}{\sqrt{N_{cm}}} \sqrt{\frac{\epsilon_0}{\mu_0}} \frac{J_l(kn_c r)}{J_l(kn_c a)},$$

$$e_{cm}^r(r) = \frac{1}{\sqrt{N_{cm}}} \frac{l}{kn_c{}^2 r} \frac{J_l(kn_c r)}{J_l(kn_c a)},$$

$$e_{cm}^\theta(r) = \frac{1}{\sqrt{N_{cm}}} \frac{i}{n_c} \frac{J_l'(kn_c r)}{J_l(kn_c a)}; \tag{A7}$$

and outside the cylinder $(r > a)$ as

$$h_{cm}^x(r) = \frac{1}{\sqrt{N_{cm}}} \sqrt{\frac{\epsilon_0}{\mu_0}} \frac{H_l^{(1)}(kr)}{H_l^{(1)}(ka)},$$

$$e_{cm}^r(r) = \frac{1}{\sqrt{N_{cm}}} \frac{l}{kr} \frac{H_l^{(1)}(kr)}{H_l^{(1)}(ka)},$$

$$e_{cm}^\theta(r) = \frac{i}{\sqrt{N_{cm}}} \frac{[H_l^{(1)}(kr)]'}{H_l^{(1)}(ka)}; \tag{A8}$$

where the superscripts x, r, and θ indicate the corresponding components, J_l is the Bessel function of the first kind of order l, $H_l^{(1)}$ is the Hankel function of the first kind of order l, and the prime $(')$ denotes differentiation with respect to the argument inside the parentheses. Here l is essentially the angular propagation constant for the specific WGM. Again, the phase factor $\exp(il\theta - i\omega t)$ has been omitted. The normalization factor N_{cm} is determined by[22]

$$1/2 \int_0^\infty \mathbf{e}_{cm} \times \mathbf{h}_{cm} \cdot \hat{\theta} \mathrm{d}r = 1. \tag{A9}$$

The normalized field patterns for the first five cylindrical WGMs can be found in Ref. 25. Applying the boundary conditions we get the following eigenvalue equation:

$$\frac{J_l'(kn_c a)}{n_c J_l(kn_c a)} = \frac{[H_l^{(1)}]'(ka)}{H_l^{(1)}(ka)}. \tag{A10}$$

Solving the eigenvalue Eq. (A10), we obtain a set of solutions with each solution corresponding to a WGM. There are two ways to solve Eq. (A10): (a) given l, solve for the eigenfrequencies; (b) given the frequency, solve for l. In the case of cw single-frequency coupling, l should be an integer as required by the coherence condition. Method (a) is usually used in this case to calculate the resonant frequencies of a specific cavity resonator. In our case, since the coupling source is a subpicosecond THz pulse, the coherence condition is not required, so l can be continuous, corresponding to a continuous frequency range. We use method (b) to solve Eq. (A10). For each given frequency, a set of solutions for l is obtained and numbered by m, the number of zeros of the transverse field component in the radial direction. This method is in fact analogous to that for the slab TM modes, where the frequency was given, to solve for the propagation constant. Here the solutions of l are generally nonintegers.

A cylindrical WGM is usually indexed by three numbers: angular index l (the angular propagation constant), radial index m (should always be an integer), and axial index h (the propagation constant in the axial direction). In our case we assume that the cylinder is longitudinally infinite, so the axial propagation constant h can be set to zero and hence dropped from the index. In addition, the angular number l is a solution to the eigenvalue equation that is determined by the frequency and radial number m. This leaves m the only number to specify a mode. In this paper, we use WG_m to indicate the WGM with radial number m, with WG_1 having one zero point located at the center of the cylinder $(r = 0)$. Its corresponding angular number should be written as l_m to indicate a mode-dependent angular propagation constant. For legibility the subscript m has been omitted for l_m in Eqs. (A7) and (A8).

3. Dispersion Relation

To analyze the coupling between the slab TM modes and cylindrical WGMs, it is necessary to know the dispersion relation of the slab TM modes and the cylindrical WGMs. For convenience we define the effective refractive indices as

$$n_{sm}(f) = \frac{c}{\nu_{sm}(f)} = \frac{c\beta_m(f)}{2\pi f} \tag{A11}$$

for the slab modes and

$$n_{cm}(f) = \frac{c}{\nu_{cm}(f)} = \frac{cl_m(f)}{2\pi a f}, \tag{A12}$$

for the WGMs,[10] where the subscript m indicates an individual mode and ν_{sm} and ν_{cm} are the phase velocities for the slab TM_m mode and the WG_m mode, respectively. Figure 9 shows the effective refractive indices for the slab TM_0, TM_1, and TM_2 modes and the first 8 cylindrical WGMs for our coupling system.

APPENDIX B: FIELD EXPRESSIONS FOR THE SLAB–CYLINDER SYSTEM

Here we give the field expressions in terms of the normalized field solutions. The fields for the isolated slab system are

$$\begin{aligned}\mathbf{E}_s(r,\theta) &= \mathbf{E}_s^t(r,\theta) + \hat{\theta}E_s^\theta(r,\theta)\\ &= [\mathbf{e}_s^t(r,\theta) + \hat{\theta}e_s^\theta(r,\theta)]\exp(i\beta z),\\ \mathbf{H}_s(r,\theta) &= \mathbf{H}_s^t(r,\theta) + \hat{\theta}H_s^\theta(r,\theta)\\ &= [\mathbf{h}_s^t(r,\theta) + \hat{\theta}h_s^\theta(r,\theta)]\exp(i\beta z). \quad \text{(B1)}\end{aligned}$$

The fields for the isolated cylinder system are

$$\begin{aligned}\mathbf{E}_c(r,\theta) &= \mathbf{E}_c^t(r,\theta) + \hat{\theta}E_c^\theta(r,\theta)\\ &= [\mathbf{e}_c^t(r,\theta) + \hat{\theta}e_c^\theta(r,\theta)]\exp(il\theta),\\ \mathbf{H}_c(r,\theta) &= \mathbf{H}_c^t(r,\theta) + \hat{\theta}H_c^\theta(r,\theta)\\ &= [\mathbf{h}_c^t(r,\theta) + \hat{\theta}h_c^\theta(r,\theta)]\exp(il\theta). \quad \text{(B2)}\end{aligned}$$

In the above equations, the lower case $\mathbf{e}(e)$ and $\mathbf{h}(h)$ represent the normalized field components. In our case, these components are

$$\begin{aligned}&\mathbf{e}_s^t(r,\theta) = \hat{r}[e_s^y(y)\cos\theta + e_s^z(y)\sin\theta],\\ &\mathbf{h}_s^t(r,\theta) = \hat{x}h_s^x(y),\\ &e_s^\theta(r,\theta) = e_s^z(y)\cos\theta - e_s^x(y)\sin\theta,\\ &h_s^\theta(r,\theta) = 0,\\ &\mathbf{e}_c^t(r,\theta) = \hat{r}e_c^r(r), \qquad e_c^\theta(r,\theta) = e_c^\theta(r),\\ &\mathbf{h}_c^t(r,\theta) = \hat{x}h_c^x(r), \qquad h_c^\theta(r,\theta) = 0, \quad \text{(B3)}\end{aligned}$$

where the Cartesian coordinates of the slab can be expressed in the cylindrical system as

$$y = r\cos\theta - (a+b), \qquad z = r\sin\theta. \quad \text{(B4)}$$

On the other hand, if we assume that the slab–cylinder system is lossless so that the relative permittivities are all real, then the modal fields propagating along the $-\theta$ direction of the isolated slab and cylinder can be written respectively, as follows[22,24]:

$$\begin{aligned}&\mathbf{E}_c^-(r,\theta) = [\mathbf{e}_c^t(r,\theta) - \hat{\theta}e_c^\theta(r,\theta)]\exp(-il\theta),\\ &\mathbf{H}_c^-(r,\theta) = [-\mathbf{h}_c^t(r,\theta) + \hat{\theta}h_c^\theta(r,\theta)]\exp(-il\theta),\\ &\mathbf{E}_s^-(r,\theta) = [\mathbf{e}_s^t(r,\theta) - \hat{\theta}e_s^\theta(r,\theta)]\exp(-i\beta z),\\ &\mathbf{H}_s^-(r,\theta) = [-\mathbf{h}_s^t(r,\theta) + \hat{\theta}h_s^\theta(r,\theta)]\exp(-i\beta z). \quad \text{(B5)}\end{aligned}$$

The total fields of the system can be formed as the modal combination of the slab and the cylinder modes as[23,24]

$$\begin{aligned}\mathbf{E}_T(r,\theta) &= a_s(z)\left[\mathbf{E}_s^t(r,\theta) + \frac{\varepsilon_s}{\varepsilon_T}\hat{\theta}E_s^\theta(r,\theta)\right]\\ &\quad + a_c(\theta)\left[\mathbf{E}_c^t(r,\theta) + \frac{\varepsilon_c}{\varepsilon_T}\hat{\theta}E_c^\theta(r,\theta)\right]\\ &= a_s(z)\left[\mathbf{e}_s^t(r,\theta) + \frac{\varepsilon_s}{\varepsilon_T}\hat{\theta}e_s^\theta(r,\theta)\right]\exp(i\beta z)\\ &\quad + a_c(\theta)\left[\mathbf{e}_c^t(r,\theta) + \frac{\varepsilon_c}{\varepsilon_T}\hat{\theta}e_c^\theta(r,\theta)\right]\exp(il\theta),\end{aligned}$$

$$\begin{aligned}\mathbf{H}_T(r,\theta) &= a_s(z)[\mathbf{H}_s^t(r,\theta) + \hat{\theta}H_s^\theta(r,\theta)]\\ &\quad + a_c(\theta)[\mathbf{H}_c^t(r,\theta) + \hat{\theta}H_c^\theta(r,\theta)]\\ &= a_s(z)[\mathbf{h}_s^t(r,\theta) + \hat{\theta}h_s^\theta(r,\theta)]\exp(i\beta z)\\ &\quad + a_c(\theta)[\mathbf{h}_c^t(r,\theta) + \hat{\theta}h_c^\theta(r,\theta)]\exp(il\theta). \quad \text{(B6)}\end{aligned}$$

ACKNOWLEDGMENTS

This work was partially supported by the National Science Foundation and the U.S. Army Research Office.

REFERENCES

1. H. M. Nussenzveig, *Diffraction Effects in Semiclassical Scattering* (Cambridge University, Cambridge, UK, 1992).
2. C. Vedrenne and J. Arnaud, "Whispering-gallery modes of dielectric resonators," IEE Proc. **129**, 183–187 (1982).
3. D. Cros and P. Guillon, "Whispering gallery dielectric resonator modes for W-band devices," IEEE Trans. Microwave Theory Tech. **38**, 1667–1674 (1990).
4. L. Collot, V. Lefèvr-Seguin, M. Brune, J. M. Raimond, and S. Haroche, "Very high-Q whispering-gallery mode resonances observed in fused silica microspheres," Europhys. Lett. **23**, 327–334 (1993).
5. S. Chiller and R. L. Byer, "High-resolution spectroscopy of whispering gallery modes in large dielectrics," Opt. Lett. **16**, 1138–1140 (1991).
6. A. T. Rosenberger, "Nonlinear optical effects in the whispering-gallery modes of microspheres," in *Operational Characteristics and Crystal Growth of Nonlinear Optical Materials*, R. B. Lal, D. O. Frazier, eds., Proc. SPIE **3793**, 179–186 (1999).
7. S. M. Spillane, T. J. Kippenberg, and K. J. Vahala, "Ultralow-threshold Raman laser using a spherical dielectric microcavity," Nature **415**, 621–623 (2002).
8. V. S. Ilchenko, P. S. Volikov, V. L. Velichansky, F. Treussart, V. Lefèvre-Seguin, J.-M. Raimond, and S. Haroche, "Strain-tunable high-Q optical microsphere resonator," Opt. Commun. **145**, 86–90 (1998).
9. P. Rabiei, W. H. Steier, C. Chang, and L. R. Dalton, "Polymer micro-ring filters and modulators," J. Lightwave Technol. **20**, 1968–1975 (2002).
10. V. S. Ilchenko, X. S. Yao, and L. Maleki, "Pigtailing the high-Q microsphere cavity: a simple fiber coupler for optical whispering-gallery modes," Opt. Lett. **24**, 723–725 (1999).
11. P. Barthia and I. J. Bahl, *Millimeter Wave Engineering and Applications* (Wiley, New York, 1984).
12. G. Annino, D. Bertolini, M. Cassettari, M. Fittipaldi, I. Longo, and M. Martinelli, "Dielectric properties of materials using whispering-gallery dielectric resonators: Experiments and perspectives of ultra-wideband characterization," J. Chem. Phys. **112**, 2308–2314 (2000).
13. D. Kajfez and P. Guillon, *Dielectric Resonators* (Artech House, Norwood, Mass., 1986).
14. G. Gallot, S. P. Jamison, R. W. McGowan, and D. Grischkowsky, "THz waveguides," J. Opt. Soc. Am. B **17**, 851–863 (2000).
15. R. Mendis and D. Grischkowsky, "Plastic ribbon THz waveguides," J. Appl. Phys. **88**, 4449–4451 (2000).
16. R. Mendis and D. Grischkowsky, "Undistorted guided wave propagation of sub-picosecond THz pulses," Opt. Lett. **26**, 846–848 (2001).
17. R. Mendis and D. Grischkowsky, "THz interconnect with low loss and low group velocity dispersion," IEEE Microw. Wire. Compon. Lett. **11**, 444–446 (2001).

18. D. Grischkowsky, S. Keiding, M. van Exter, and Ch. Fattinger, "Far-infrared time-domain spectroscopy with terahertz beams of dielectrics and semiconductors," J. Opt. Soc. Am. B **7**, 2006–2015 (1990).
19. R. W. Shaw, W. B. Whitten, M. D. Barnes, and J. M. Ramsey, "Time-domain observation of optical pulse propagation in whispering-gallery modes of glass spheres," Opt. Lett. **23**, 1301–1303 (1998).
20. J. Zhang and D. Grischkowsky, "Whispering-gallery mode terahertz pulses," Opt. Lett. **27**, 661–663 (2002).
21. A. W. Snyder, "Coupled-mode theory for optical fibers," J. Opt. Soc. Am. **62**, 1267–1277 (1972).
22. A. W. Snyder and J. D. Love, *Optical Waveguide Theory* (Chapman & Hall, London, 1983).
23. S.-L. Chuang, "A coupled mode formulation by reciprocity and a variational principle," J. Lightwave Technol. **LT-5**, 5–15 (1987).
24. Q. Han, Y. Kogami, Y. Tomabechi, and K. Matsumura, "Coupling characteristics of eccentric arranged dielectric disk and ring," IEEE Trans. Microwave Theory Tech. **44**, 2017–2024 (1996).
25. J. Zhang, Ph.D. thesis, "A cylindrical dielectric whispering-gallery mode terahertz cavity coupled with a dielectric slab waveguide" (Oklahoma State University, Stillwater, Oklahoma, 2002).
26. M. L. Gorodetsky and V. S. Ilchenko, "Optical microsphere resonators: optimal coupling to high-Q whispering-gallery modes," J. Opt. Soc. Am. B **16**, 147–154 (1999).
27. J. D. Stratton, *Electromagnetic Theory* (McGraw-Hill, New York, 1941).